High-Valence W^{6+} Ions Boost Cr^{2+} Activity in $CrWO_4$ for Ideal Water Oxidation

Chanseok Kim, Dasom Jeon, Nayeong Kim, Jungki Ryu,* and Jun Hee Lee*

Electrocatalytic activity of multi-valence metal oxides for oxygen evolution reaction (OER) arises from various interactions among the constituent metal elements. Although the high-valence metal ions attract recent attentions due to the interactions with their neighboring $3d$ transition metal catalytic center, atomic-scale explanations for the catalytic efficiencies are still lacking. Here, by employing density functional theory predictions and experimental verifications, unprecedented electronic isolation of the catalytic $3d$ center (M^{2+}) induced by the surrounding high-valence ions such as W^{6+} is discovered in multivalent oxides MWO_4 (M = Ti, V, Cr, Mn, Fe, Co, Ni, Cu, and Zn). Due to W^{6+}'s extremely high oxidation state with the minimum electron occupations (d^0), the surrounding W^{6+} blocks electron transfer toward the catalytic M^{2+} ions and completely isolates the ions electronically. Now, the isolated M^{2+} ions solely perform OER without any assistant electron flow from the adjacent metal ions, and thus the original strong binding energies of Cr with OER intermediates are effectively moderated. Through exploiting "electron isolators" such as W^{6+} surrounding the catalytic ion, exploring can be done beyond the conventional materials such as Ni- or Co-oxides into new candidate groups such as Cr and Mn on the left side of the periodic table for ideal OER.

C. Kim, D. Jeon, N. Kim, J. Ryu, J. H. Lee
Department of Energy Engineering
School of Energy and Chemical Engineering
Ulsan National Institute of Science and Technology (UNIST)
50 UNIST-gil, Ulju-gun, Ulsan 44919, Republic of Korea
E-mail: jryu@unist.ac.kr; junhee@unist.ac.kr
J. Ryu
Graduate School of Carbon Neutrality
Ulsan National Institute of Science and Technology (UNIST)
50 UNIST-gil, Ulju-gun, Ulsan 44919, Republic of Korea
J. H. Lee
Graduate School of Semiconductor Materials and Devices Engineering
Ulsan National Institute of Science and Technology (UNIST)
50 UNIST-gil, Ulju-gun, Ulsan 44919, Republic of Korea

1. Introduction

Development of new cost-effective and highly active catalysts for electrochemical energy conversion and storage is a prime challenge to address climate change issues. The oxygen evolution reaction (OER) is particularly important for the effective utilization of renewable energy and electricity using electrochemical devices such as H_2–O_2 fuel cells,[1] metal–air batteries,[2,3] and water electrolyzers.[4,5] Transition metal (TM) oxides and their derivatives are explored as OER electrocatalysts alternative to expensive noble metal-based ones.[6–8] Conventionally, late $3d$ TMs (Fe, Co, and Ni) are considered promising catalyst candidates for OER due to their abundance, low cost, and electrochemical activities. Their activity can be tailored by controlling structure, morphology, dopants, and defects.[9,10] Still, novel catalyst design strategies and better theoretical understanding of microscopic mechanisms are urgently required to discover new catalysts beyond Co- or Ni-based ones.

Tungstate is emerging since it is abundant and can synergistically enhance the OER activity of other transition metal elements.[11–13] According to the previous papers, transition-metal-tungstates (TMTs) show good electrochemical OER performance.[10,11,14–16] However, the reported studies limit the role of W as an auxiliary modifier to enhance structural stability[17,18] or electrochemical activity of other adjacent metal elements.[19] Moreover, in-depth understanding of the underlying mechanism is still lacking.

In this study, we systematically analyzed the role of W in TMTs for OER. For the computational analysis, six TMTs, monoclinic MWO_4 (M = Mn, Fe, Co, Ni, Cu, and Zn), are considered because they are reported as excellent catalysts for water splitting.[16] and three more TMTs ($TiWO_4$, VWO_4, $CrWO_4$) are additionally investigated to determine volcano-type relation about OER activity. Strikingly, we uncover $CrWO_4$ shows the best OER performance among the TMTs investigated, and our prediction was experimentally supported. Interestingly, when the active sites ($3d$ TMs) are surrounded by the highly oxidized tungsten ions (W^{6+}) with minimum electron occupation (d^0), W^{6+} completely block any electron flow toward the active $3d$ sites and now the active site shows isolated single-atom-like catalytic properties.[20,21] with

**ADVANCED
SCIENCE NEWS**

www.advancedsciencenews.com
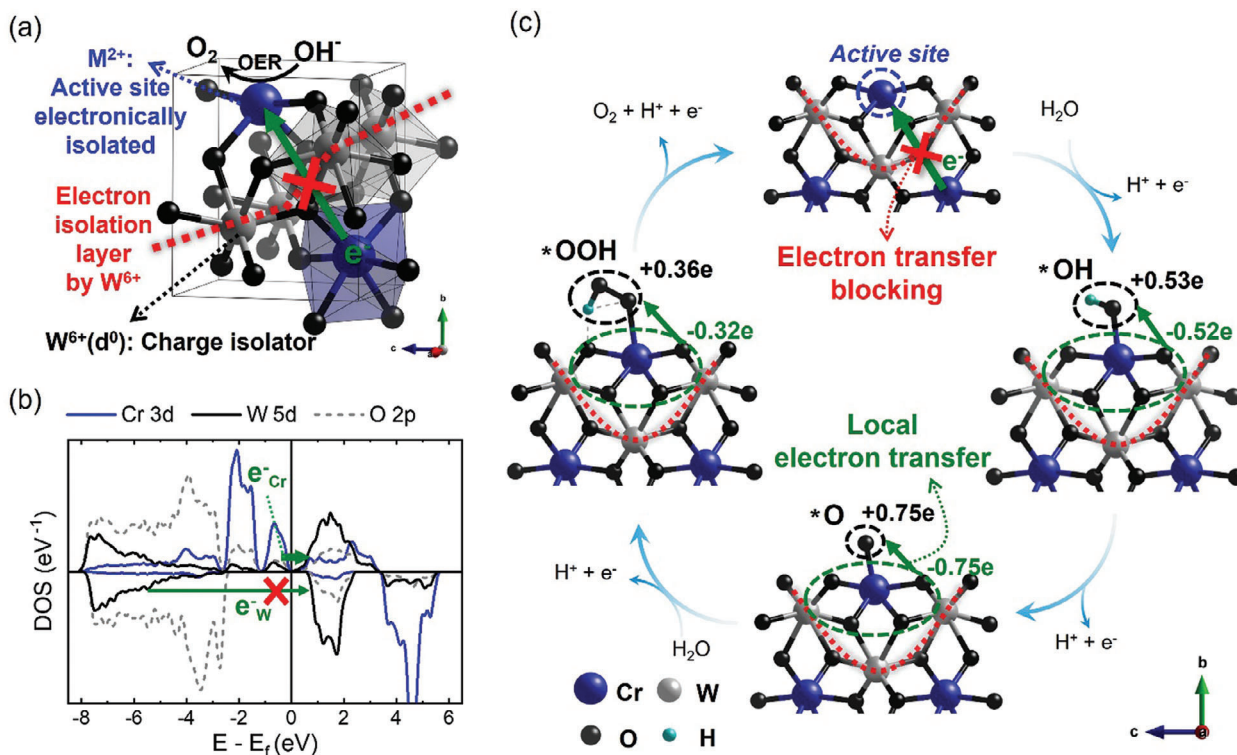
NANO · MICRO

small

www.small-journal.com

Figure 1. a) Crystal structure of monoclinic MWO_4 (M = Ti, V, Cr, Mn, Fe, Co, Ni, Cu, Zn). Red dotted line denotes the electron transfer blocking by W^{6+} ions. b) Projected density of state (DOS) of $CrWO_4$. W has relatively low energy level (black solid line) of d-orbital compared to Cr (blue solid line). Therefore, the electron excitation occurs mainly in Cr rather than W because transferring electrons through W is energetically unfavorable. Due to this d orbital energy difference, W is electronically inactive in systems where Cr and W are mixed in a 1:1 ratio, thereby producing a bulk material having Cr as a single-atom catalyst. c) Structure of different OER adsorbents ($^*OH$, $^*O$, and $^*OOH$) on crystalline $CrWO_4$ (010) that is A ion terminated surface. Electron transfer blocking layer is marked with red dotted lines. Due to the electron blocking toward Cr on surface by W, Cr solely performs OER.

its extremely localized $3d$ electrons. Without any assistant electron flow toward Cr, the originally strong binding energies of Cr with OER intermediates ($^*OH$, $^*O$, $^*OOH$) are moderated for ideal OER. This W^{6+} electronically isolates the $3d$ electrons of the transition metal active site and makes the contribution of the d-band center more significant than the previously known p-band center.[22–24] for OER activity. We show that this electron isolation strategy using the surrounding high oxidation state ions will be a novel route to expand OER material candidates beyond the conventional late $3d$ TMs to the early $3d$ TMs.

2. Results and Discussion

2.1. Electron Isolation Mechanism in Monoclinic Catalysts

Figure 1 shows how the electron isolator (W^{6+}) blocks electron transfer to the active sites in the TMTs, $M^{2+}W^{6+}O_4$ (M = Ti, V, Cr, Mn, Fe, Co, Ni, Cu, and Zn). In the TMTs, W has 6+ oxidation state, and the neighbor $3d$ TMs have 2+ oxidation state. This extremely high oxidation state of W lowers the total energy of the W electrons than that of the surrounding $3d$ TMs electrons. This low-energy state below the Fermi level makes it difficult for the electrons in W^{6+} to participate in the electrochemical reaction (Figure 1b; Figure S1, Supporting Information). Since the low energy W^{6+} ions hardly participate in OER and further geometrically surround the active $3d$ TMs site as shown in Figure 1a, the $3d$

TM ions are electrically and structurally isolated by the W^{6+} and thus solely perform the OER reaction. When this type of monoclinic catalyst is involved in OER, $3d$ TM ions engage as active sites like single-atom catalytic systems. This postulation can be verified by tracking the theoretically estimated number of electrons that change with respect to the OER cycle. Figure 1c shows the electron transfer resulting by OER on the $CrWO_4$ surface. When the OER intermediates ($^*OH$, $^*O$, and $^*OOH$) are attached to Cr on the surface, electrons are transferred only from CrO_4 (green dotted circle) to the intermediates (black dotted circle). The electron extractions from the local CrO_4 geometry (−0.52, −0.75, and −0.32e, green numbers) are strikingly similar to the electron accumulation into the intermediates for $^*OH$, $^*O$, and $^*OOH$ intermediates, respectively (+0.53e, +0.75e, and +0.36e, black number). This spatially localized transfer only from CrO_4 unit might be attributed to the fact that MWO_4 is an insulator. However, the local electron transfer does not appear in $SrTiO_3$ and TiO_2, which are also insulating oxide materials. (Figure S2, Supporting Information)

2.2. OER Activity Prediction and Scaling Law Analysis About MWO_4 with DFT

Figure 2 shows the scanned OER standard free energy diagram of TMTs with $3d$ TMs, monoclinic MWO_4 (M = Ti, V, Cr, Mn, Fe,

2400114 (2 of 9)

ADVANCED
SCIENCE NEWS

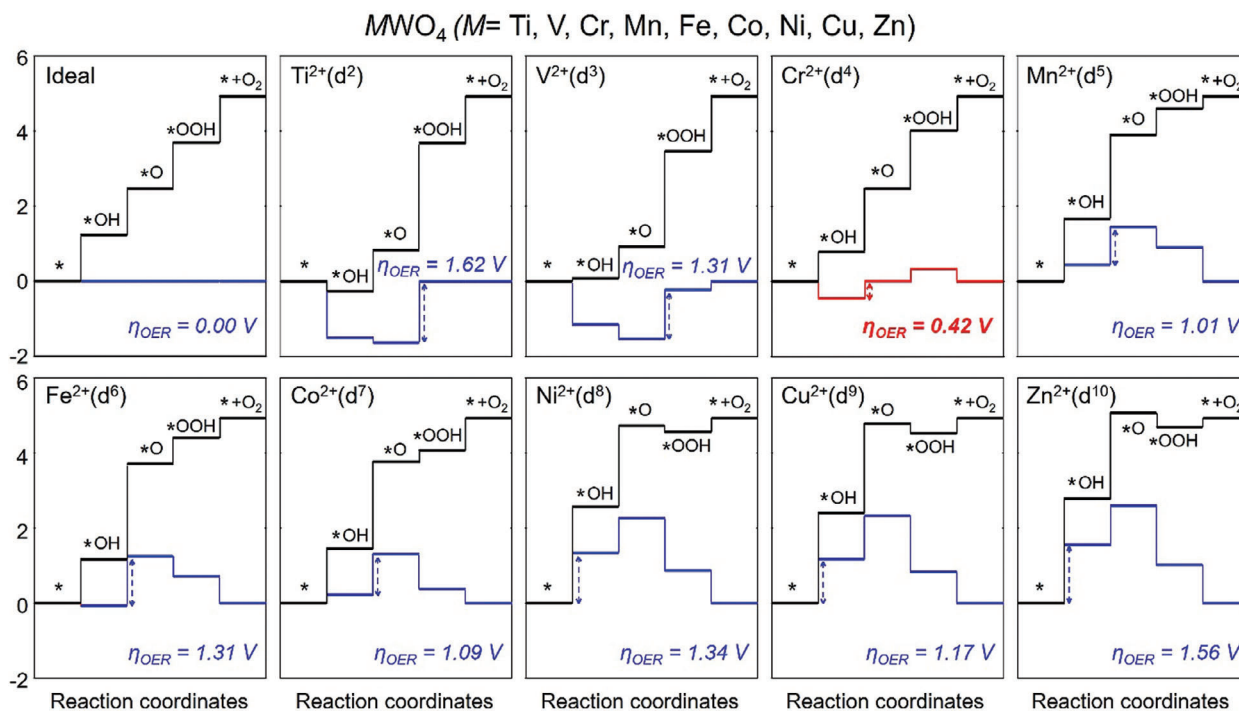www.advancedsciencenews.com

NANO · MICRO
small
www.small-journal.com

Figure 2. Standard free energy diagram of ideal monoclinic MWO_4 (M = Ti, V, Cr, Mn, Fe, Co, Ni, Cu, and Zn) for the OER at zero potential (U = 0 V), and equilibrium potential for oxygen evolution (U = 1.23 V). η_{OER} is overpotential of potential determining step. Note that $CrWO_4$ shows the lowest η_{OER}.

Co, Ni, Cu, and Zn). For ScWO₄, the surface structure distorted due to strong interaction between Sc and OER adsorbent oxygen (*O), necessitating its exclusion from the comparison group. The (010) surface terminated with 3d TM is recognized as the active site for OER in MWO_4.[25] As depicted in Figure S3 (Supporting Information), the creation of the (010)M surface necessitates the cleavage of only two M=O bonds. In contrast, the formation of all other surfaces requires the breaking of W=O bonds. Within the MWO_4 crystal structure, M and W exist in the +2 and +6 oxidation states, respectively. This disparity in oxidation states signifies a significantly stronger bond between W and O compared to M and O. Consequently, the cleavage of W=O bonds necessitates a greater expenditure of energy compared to the cleavage of M=O bonds. The method was developed by Nørskov and his co-workers.[26] is applied to analyze the complete OER process. The potential determining step for Ti and V is the 3rd OER step (*O + H₂O → *OOH + H⁺ + e⁻), for Cr, Mn, Fe, and Co is the 2nd OER step (*OH → *O + H⁺ + e⁻), and for Ni, Cu, and Zn is the 1st OER step (* + H₂O → *OH + H⁺ + e⁻). Through this tendency, as the number of 3d orbital electrons increases, the overall energy to adsorb OER intermediate species decreases. The minimum theoretical overpotential that is the best for OER among them is 0.42 V of CrWO₄. In contrast to previous results that the best OER originates from Co²⁺/Co³⁺,[8] Ni²⁺/Ni³⁺,[19] or Fe²⁺/Fe³⁺,[19] we show that Cr²⁺ shows the best performance with W⁶⁺ in the multivalent oxide system.

The data described in Figure 2 is utilized to predict the linear correlation of the binding energies of *OH, *O, and *OOH on TMT surfaces.[27] As shown in **Figure 3a,b**, we obtained a wide range of binding energies with the clear linear relations of *OH

and *OOH about the *O binding energy, ΔE_O, respectively. The slope (0.66) of the linear relation ($\Delta E_{OH} = 0.66 \, \Delta E_O - 1.17$ eV) for TMT surface is almost identical to that (0.61) found for the rutile type (AO₂) oxide surface,[27] reflecting the double bond nature of *=O and the single bond nature of *=OH. (Figure 3a). According to Nørskov and his co-workers,[27,28] *OOH has also single bond nature with the slopes of 0.53 for metals and 0.64 for rutile oxides. However, TMT surfaces show a lower slope (0.26), denoting *OOH makes a weaker bond than a single bond (Figure 3b).

We predict CrWO₄ would exhibit an excellent bifunctional activity for both OER and ORR (oxygen reduction reaction) with W⁶⁺ in the oxide as shown in Figure 3c. With the determined linear relations between the binding energies of *O, *OH, and *OOH intermediates, the OER activity of TMTs is plotted as a function of *O binding energy (ΔE_O) (Figure 3c). The activity, defined as the negative change of the free energy ($-\Delta G$), is shown for the four OER reaction steps. The closer to the dotted line (1.23 V) inside the gray area, the more OER active at the bottom and ORR active at the top. Compared to the theoretical equilibrium potential of 1.23 V, it is possible to find oxides associated with very small overpotentials at $\Delta E_O = 2.25$ eV for OER and $\Delta E_O = 2.55$ eV for ORR. Strikingly, CrWO₄ would exhibit bifunctional activity favoring both OER and ORR.

2.3. Simulated OER Activity Trend Validation with Experimental OER Activity Data

Figure 4a shows overpotential (η_{OER}) as a function of ΔE_O for the TMTs with that of perovskite oxides sourced from reference

ADVANCED
SCIENCE NEWS

www.advancedsciencenews.com
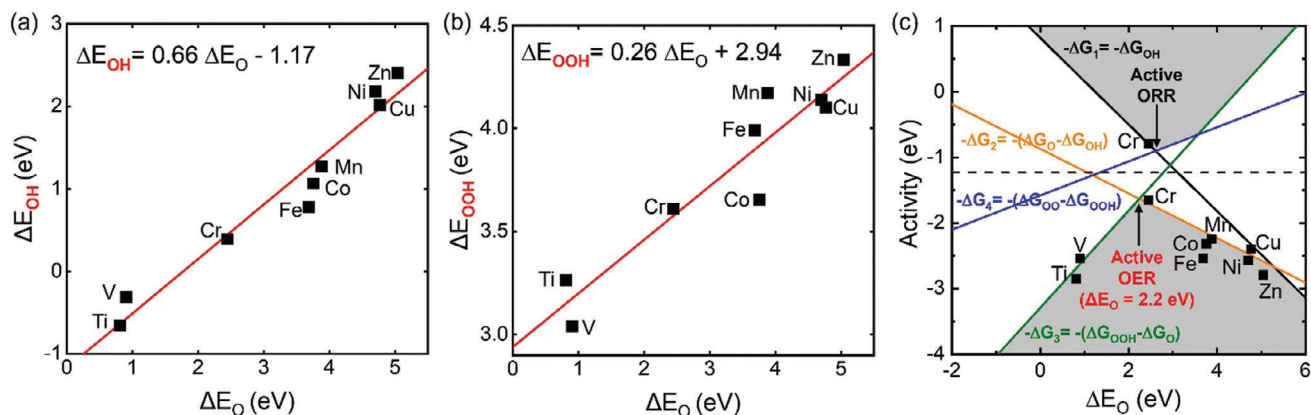
NANO · MICRO
small
www.small-journal.com

Figure 3. Scaling relationship between the binding energy of a) $^*O$ and $^*OH$, and b) $^*O$ and $^*OOH$ on 3d TM-based tungstates (010) surfaces. The linear fittings to the data points are: $\Delta E_{OH} = 0.66 \Delta E_O - 1.17$ eV and $\Delta E_{OOH} = 0.26 \Delta E_O + 2.94$ eV. c) The theoretical activity of the four electron transferring steps of oxygen evolution is described as a function of the oxygen binding energy The y-axis is the activity defined as ΔG of the different reaction steps, calculated from the linear relations: $\Delta G_1 = \Delta G_{OH} - \Delta G_{water} = \Delta E_{OH} + 0.35$ eV, $\Delta G_2 = \Delta G_O - \Delta G_{OH} = \Delta E_O + 0.05$ eV $- \Delta E_{OH} - 0.35$ eV, $\Delta G_3 = \Delta G_{OOH} - \Delta G_O = \Delta E_{OOH} + 0.40$ eV $- \Delta E_O - 0.05$ eV, $\Delta G_4 = \Delta G_{OO} - \Delta G_{OOH} = 4.96$ eV $- \Delta E_{OOH} - 0.40$ eV. The resulting volcano is indicated with the dark gray areas. The best material would fall on the horizontal black dashed line representing the equilibrium potential of 1.23 eV.
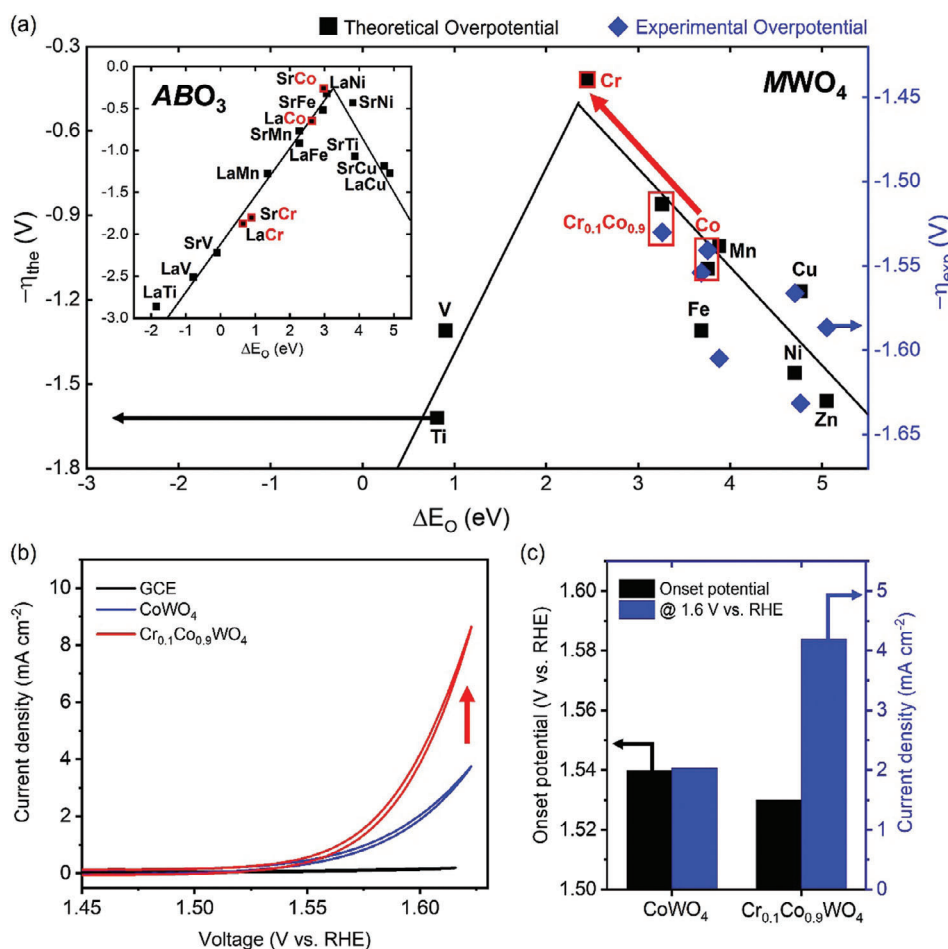

Figure 4. a) Volcano relation obtained from DFT calculated theoretical overpotentials (black rectangular) for the OER on monoclinic MWO$_4$ (010) surfaces. The inset shows a volcano plot for OER in perovskite ABO$_3$. The negative theoretical overpotential was plotted against the oxygen binding energy of the ΔE_O. The blue rhombus is the experimental onset potential in alkaline media (room temperature, pH 13) b) Cyclic voltammograms of CoWO$_4$ and Cr$_{0.1}$Co$_{0.9}$WO$_4$ in 1 M KOH (pH 14), c) Values of onset potential and current density of CoWO$_4$, Cr$_{0.1}$Co$_{0.9}$WO$_4$.

**ADVANCED
SCIENCE NEWS**

www.advancedsciencenews.com

**NANO · MICRO
small**

www.small-journal.com

paper.[26] (Figure 4a; inset). Generally, among the 3d TM-based oxide materials, the OER active materials are based on Co or Ni since their appropriate binding energy with OER intermediates (*OH, *O, *OOH). In the case of perovskite oxides (Figure 4a; inset), $SrCoO_3$ and $LaNiO_3$ show excellent performance, while Cr-based $LaCrO_3$ and $SrCrO_3$ show poor performance. However, in the TMT system, $CrWO_4$ is the best OER catalyst. To evaluate the reliability of this study, the calculation results are matched with the reported experimental OER onset potentials.[16] (Figure 4a; blue rhombus). Because Cr^{2+} is difficult to be stabilized, there is no $CrWO_4$ OER report. For the Cr-based TMT catalytic activity analysis, 10% Cr doping strategy was introduced in $CoWO_4$ ($Cr_{0.1}Co_{0.9}WO_4$) after optimization of the amount of Cr in $CoWO_4$ (Figure S4, Supporting Information). Before assessing the performance, we conducted XPS and XRD measurements to confirm the successful chemical synthesis of catalysts (Figures S5 and S6, Supporting Information). The XPS results confirmed the presence of W, Co, Cr, and O in $Cr_{0.1}Co_{0.9}WO_4$. The XRD pattern also revealed that $Cr_{0.1}Co_{0.9}WO_4$ exhibited crystalline peaks characteristic of both $CoWO_4$ and $CrWO_4$. Figure 4b shows the CV curves of $CoWO_4$ and $Cr_{0.1}Co_{0.9}WO_4$ in 1 M KOH (pH ≈14). Obviously, the OER activity of $CoWO_4$ is significantly improved by the introduction of Cr doping. The onset potential of $Cr_{0.1}Co_{0.9}WO_4$ is reduced compared to $CoWO_4$. At 1.6 V vs. RHE, the current density of $Cr_{0.1}Co_{0.9}WO_4$ is 4.20 mA cm^{-2}, more than twice that of $CoWO_4$ (2.04 mA cm^{-2}) (Figure 4c). To compare the activity of catalysts containing other transition metals, we also prepared $NiWO_4$ and $FeWO_4$ (Figure S7, Supporting Information) and found that $NiWO_4$ and $FeWO_4$ showed a negligible catalytic activity. Based on the analysis of the polarization curves, we calculated the Tafel slopes to assess the OER kinetics. $Cr_{0.1}Co_{0.9}WO_4$ exhibited a lower Tafel slope of 60.01 mV dec^{-1} compared to a blank GCE (474.39 mV dec^{-1}) and $CoWO_4$ (73.29 mV dec^{-1}) (Figure S8, Supporting Information). This finding suggests that the rate-determining step for OER by $Cr_{0.1}Co_{0.9}WO_4$ is the formation of *OOH.[29] To indirectly demonstrate the role of W^{6+} in the OER performance, we measured the polarization curves of Cr oxide and Co oxide without W (Figure S9, Supporting Information). They showed no activity for OER, aligning with computational findings and indicating crucial role of W^{6+} in facilitating the OER performance. To further investigate the OER kinetics, we conducted electrochemical impedance spectroscopy. In the Nyquist plots, $Cr_{0.1}Co_{0.9}WO_4$ showed a markedly lower charge transfer resistance (R_{ct}) compared to $CoWO_4$, indicating rapid electron transfer between electrode and electrolyte (Figure S10, Supporting Information). The electrochemically active surface area (ECSA) was determined by measuring the double-layer capacitance (C_{dl}). Based on the CV curves in the non-Faradaic region, the C_{dl} value of $Cr_{0.1}Co_{0.9}WO_4$ and $CoWO_4$ were calculated to be 170.80 and 118.39 mF cm^{-2}, respectively, demonstrating that $Cr_{0.1}Co_{0.9}WO_4$ has a higher bilayer capacity (Figure S11, Supporting Information). Despite $Cr_{0.1}Co_{0.9}WO_4$ having the highest ECSA value, its current density remained the highest among the ECSA-normalized polarization curves, indicating its exceptional electrochemical OER performance (Figure S12, Supporting Information). To evaluate the stability of $Cr_{0.1}Co_{0.9}WO_4$, we conducted chronopotentiometry (CP) for 100 h (Figure S13, Supporting Information). $Cr_{0.1}Co_{0.9}WO_4$ maintained stable performance with negligible voltage fluctuations throughout the ex-

tended OER test. In addition, Figure S14 (Supporting Information) shows the ORR activity of $CoWO_4$ and $Cr_{0.1}Co_{0.9}WO_4$. As with OER, the ORR performance of $CoWO_4$ is enhanced by 10% Cr doping. These OER and ORR experimental results are consistent with the bifunctionality of Cr-based TMT predicted by the scaling relationship in Figure 3c.

2.4. Systematic Analysis About Mechanism and Novel OER Activity Descriptor

For a mechanistic picture of TMT OER, the Bader charge distribution before and after oxygen adsorption, and the corresponding differential charge density were investigated (**Figure 5**). As illustrated in Figure 5a,c that shows Bader charge distribution, the adsorbed oxygen gained 0.75e (0.47e) electron from $CrWO_4$ ($CoWO_4$) surface. The source is the oxygen adsorbed Cr (Co) ion and four oxygen ions around it. In Figure 5b,d), which is visualizing the electron-charge difference between before and after oxygen adsorption, the Cr (Co) and the neighboring only four oxygen ions participated in the OER absorbate adsorption step as if they are single-atom catalysts that are electrically unaffected by the surroundings. This electrical isolation phenomenon occurs at the boundary of the W^{6+} ions surrounding the surface CrO_4 (CoO_4). However, in the case of $LaCoO_3$ perovskite oxide (Figure 5e), the adsorbed oxygen gained 0.41 electron from $LaCoO_3$ surface, and its source is distributed to all Co and O ions down to the three layers of $LaCoO_3$ surface except La ions (Figure 5f). Notably, similar global electron flow patterns were observed on the OER surfaces of Cr_2O_3 and Co_3O_4 (Figure S15, Supporting Information), indicating that W plays a critical role in the local electron flow observed for TMT-based OER.

The difference between the local electron flow of TMT and the global electron flow of perovskite affects the different degrees of OER contribution dominance between TM and O. In the TMTs, the electron donation toward the adsorbed intermediate molecules is mainly originated from the d-orbital of TMs as shown in the huge local amount electron extraction (−0.47e) from Cr^{2+} whereas in perovskite oxides, the oxygen p-orbital mainly contributes.[22,30,31] So, we develop a new descriptor to effectively describe the degree of OER contribution dominance between the transition metal ion and oxygen atom in TMT.

To systematically support the electrical contribution of d- and p-orbitals for OER activity, we conducted a study involving regression analysis of the oxygen binding energy (ΔE_O) values, using the metal d-band center (M_d) and oxygen p-band center (O_p) as descriptive parameters. The M_d (O_p) descriptor is defined as the weighted projected density of states (pDOS) center of 3d-orbital (2p-orbital) of TM ions (lattice oxygen ions), which can be described by Equation 1:

$$M_d\left(O_p\right) = \frac{\int_{-\infty}^{E_f} E \times \rho_{3d(2p)} dE}{\int_{-\infty}^{E_f} \rho_{3d(2p)} dE} \tag{1}$$

$\rho_{3d(2p)}$ is the pDOS for 3d (2p)-orbital of the atoms at energy E and E_f is the Fermi level of the structure. Due to the limited number of samples (MWO_4, M = Ti, V, Cr, Mn, Fe, Co, Ni, Cu, and Zn, with their respective values are shown in Figure S16,
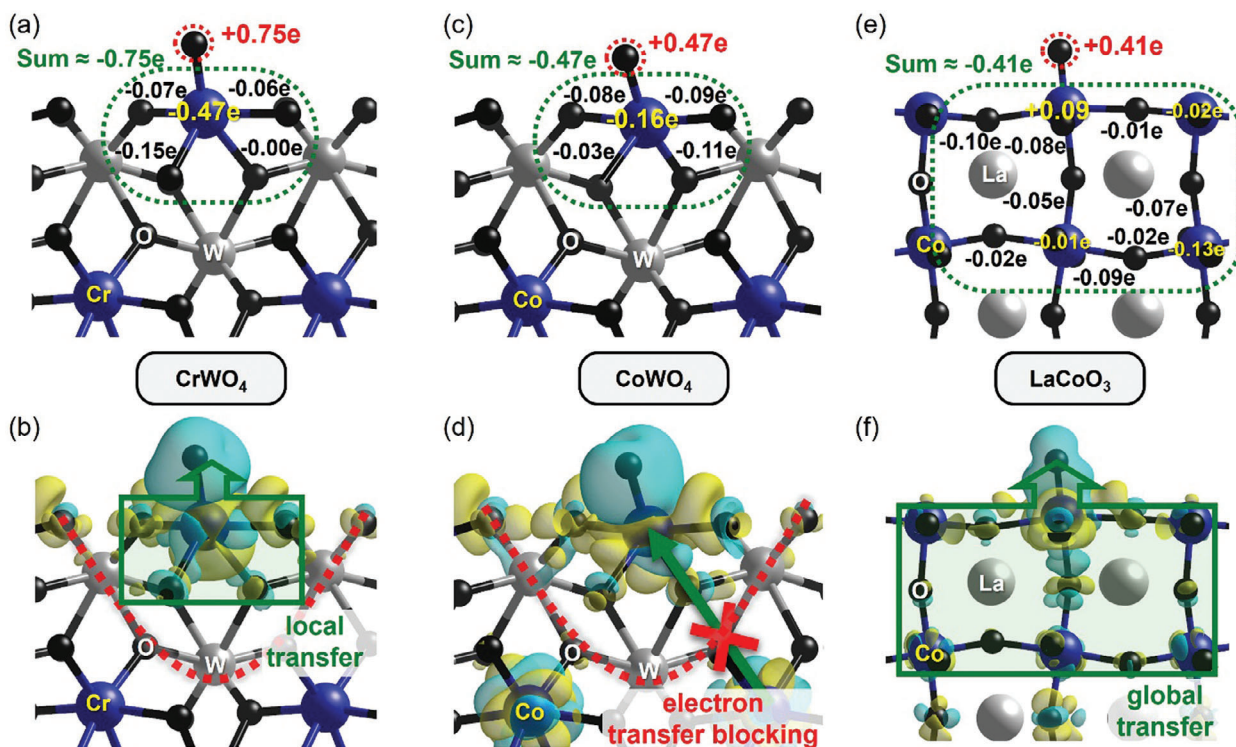
Figure 5. The Bader charge distribution before and after adsorption (top), and the corresponding differential charge density (bottom) of a,b) monoclinic (010) $CrWO_4$, c,d) monoclinic (010) $CoWO_4$, and e,f) Perovskite (100) $LaCoO_3$. The black, yellow, and red numbers are the Bader charge of lattice oxygens, 3d metals (Cr and Co), and adsorbed oxygen ions, respectively. The 'Sum' values in green are the net Bader charge data in the volume enclosed by the green dashed line, which is consistent with the charge difference of the adsorbed oxygen ion. The cyan and yellow surfaces correspond the charge gain and lost regions, respectively (iso-value, 0.002). The electron transfer blocking layer by W ions is marked with red dotted line and electron transferring feature is marked with green arrow.

Supporting Information), we performed a regression test with several combinations of O_p and M_d (Figure S17, Supporting Information). Interestingly, O_p/M_d (**Figure 6a**, RMSE = 0.29, MAE = 0.25, and R^2 = 0.96) emerged as the best descriptor of the 96% linear relationship with ΔE_O than single descriptors, O_p

(RMSE = 0.47, MAE = 0.43, and R^2 = 0.90), and M_d (RMSE = 0.91, MAE = 0.80, and R^2 = 0.63), which are reported descriptors in previous papers.[22–24] Additionally, we conducted regression tests with other parameters, M_d-O_p (one parameter, RMSE = 0.63, MAE = 0.56, and R^2 = 0.83), and M_d &
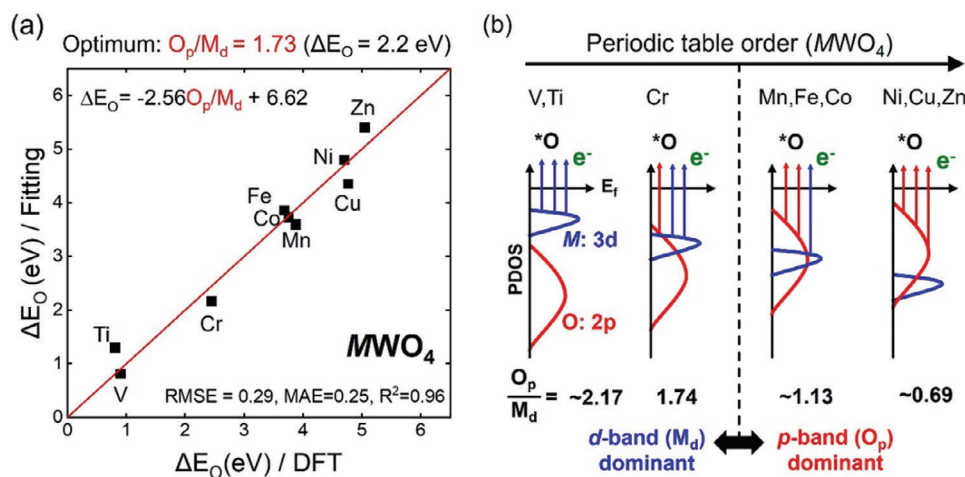

Figure 6. a) Parity plot between predicted by regression model and DFT-calculated ΔE_O values for 3d TM-based monoclinic tungstate oxides (MWO_4) is depicted. b) Schematic representation to express the physical meaning of O_p/M_d is depicted. In DOS of 3d TM, the shape of 3d orbital and 2p orbital, and their contribution to the adsorbate (*O) are related to the O_p/M_d value.

ADVANCED
SCIENCE NEWS

www.advancedsciencenews.com

NANO · MICRO

small

www.small-journal.com

O_p (two parameters, RMSE = 0.46, MAE = 0.44, and R^2 = 0.91), based on the previous papers.[31–33] that emphasize the importance of hybridization of metal and oxygen ions. However, both two-descriptor combinations were found to be less accurate than O_p/M_d. It's worth noting that O_p/M_d also encapsulates information about the degree of hybridization between metal and oxygen ions; the closer to O_p/M_d = 1, the more hybridized. Note that O_p and M_d are expressed as negative numbers, indicating how far the entire orbital position is from E_f. By dividing O_p by M_d, we obtain a unitless value that is independent of the energy scale of a specific material, allowing for a normalized representation of the band structure for various TMs. For early (late) 3d TMs such as V and Ti (Ni, Cu, and Zn), O_p/M_d is ≈2.17 (0.69), signifying that the d-orbital level is close (far) to E_f≈2 times compared to the p-orbital level. This indicates that d-orbital (p-orbital) has dominant role in the electron transfer to the O adsorbate (Figure 6b). According to the theoretical OER activity for TMTs (Figure 3c), the highest OER activity is achieved when the oxygen binding energy is 2.2 eV, corresponding to an O_p/M_d value of 1.73. This implies that in the TMT system, the optimal degree of hybridization between p-orbital and d-orbital is 1.73 (indicating less hybridization), and d-orbital is closer to E_f than p-orbital. Consequently, $CrWO_4$ with an O_p/M_d value of 1.74 is identified as the most optimized material within the TMT system.

To explore the versatility of O_p/M_d, we referred to the reported oxygen-binding energy data of perovskites.[26] and calculated the O_p/M_d value for each cited perovskite. As depicted in Figure S18 (Supporting Information), the regression results for perovskites are less accurate (RMSE = 0.78, MAE = 0.69, and R^2 = 0.79) than those for TMTs (RMSE = 0.29, MAE = 0.25, and R^2 = 0.96). According to Nørskov et al.,[26] the optimal ΔE_O value for perovskite's OER activity is ≈3.0 eV, corresponding to an O_p/M_d value of 0.48. This value (0.48) indicates that the oxygen p-orbital is energetically closer to Fermi energy than the metal d-orbital, similar to the orbital configuration observed in late TMs (Ni, Cu, and Zn), as depicted in Figure 6b. This suggests that, for the optimal OER of perovskites, electron donation to the reactant molecules should be primarily driven by the oxygen p-orbital, as reported previously.[22,24] However, reported papers have a limitation of analyzing mainly late 3d TMs (p-band dominant) such as Fe, Co, and Ni, omitting the analysis of early 3d TMs (d-band dominant) such as V, Ti, and Cr. Therefore, it is noteworthy that the O_p/M_d of perovskite shows a clear 79% linear relationship with ΔE_O from V to Zn. These results strongly suggest that the O_p/M_d descriptor has the potential to describe the optimal orbital states within various oxide systems for achieving the highest OER activity. Just as the d-band dominant form (O_p/M_d ≈ 1.73) of TMT and the p-band dominant form (O_p/M_d ≈ 0.48) of perovskite are the most optimized orbital states for OER.

3. Conclusion

In the present study, electronic, structural, and surface properties of 3d TM-based tungstates, monoclinic MWO_4 (M = Ti, V, Cr, Mn, Fe, Co, Ni, Cu, and Zn), are systematically investigated. It was confirmed that the 3d TM active site is surrounded by the highly oxidized W^{6+} with minimum electron occupation (d^0), resulting in electronic isolation of the catalytically active atom. Since W^{6+} block any electron transfer toward M^{2+} during OER,

M^{2+} solely transfer electrons to OER intermediates, resulting in an overall weakening of its binding energy with these intermediates. With the universally weakened binding energies, Cr, which showed strong binding to OER intermediates in perovskites, is now expected to exhibit the optimal biding and the best OER performance among the 3d-transition metal ions. With the investigation of universal scaling relationship between the binding energy of *OOH and *OH in TMTs, Cr-based TMT was identified as the most OER active. Our discovery uncovers Cr as a main catalytic active site in contrast to previous studies showing Cr as an auxiliary site for H_2O adsorption,[34] p-band center tuning assistance,[35] or electrochemically accessible surface area growth.[36,37] The superior performance of the early transition metal such as Cr over Co and Ni is an interesting finding because, for most TM-based oxides, materials based on the late TMs such as Co and Ni show major OER activity. Even in the other 3d metal-based system with W, it has been reported that Fe^{2+} is more efficient than Co, Ni, and Cu.[19] However, our work demonstrates that Cr^{2+}, which is almost left side of the periodic table, can exhibit the best performance with complete electronic isolation by W^{6+}. We conject that the isolation arises because the active site (M) of MWO_4 is completely surrounded by W^{6+}, while the M in the previous literature.[19] is partially surrounded by the less doped W. This form of electronic contribution can be described by the new descriptor O_p/M_d applicable to both TMT and perovskite oxides. This study enables us to move beyond the conventional material candidate group of OER catalysts based on late TMs such as Ni and Co and expand our scope to new material candidate groups, including early TMs like Cr.

4. Experimental Section

DFT Computational Details: All electronic structure calculations were performed using the Vienna Ab initio Structure Package (VASP).[38,39] GGA-PBE exchange-correlation functional[40] of DFT was used along with projector-augmented wave (PAW) pseudopotentials to deal with the core−valence interactions, and cutoff energy for pseudopotential was set to 500 eV. MWO_4 (M = Ti, V, Mn, Fe, Co, Ni, Cu, and Zn) was modeled as a monoclinic structure, and the stable (010).[25] surface slab was generated with one layer of MWO_4 fixed as the bulk phase and another three layers relaxed as the surface phase. A vacuum layer of at least 16 Å was added to rule out an imaginary interaction between repeating slabs in the z-direction. The geometry relaxations were given until the residual force on unconstrained atoms became less than 0.01 eV Å^{-1} with (6 × 6 × 1) Monkhorst−Pack mesh. The optimized structures of bare MWO_4 surfaces and surfaces with adsorbed OER intermediates *, *OH, *O, and *OOH (asterisk denoting adsorbed species) were simulated for OER free energy calculation. The GGA+U method was also applied to reduce the self-interaction error and improve the description of correlation effects. For the GGA+U calculation, the standard Dudarev implementation was used.[41] where the on-site Coulomb interaction for the localized orbitals is parametrized by U_{eff} = U − J using the PBE functional. The optimized effective interaction parameter U_{eff} for the metal atoms was applied in MWO_4 (U_{eff} = 4.0, 3.1, 3.5, 3.9, 4.0, 4.5, 6.0, 4.0, and 4.7 eV for Ti,[42] V,[43] Cr,[43] Mn,[43] Fe,[43] Co,[25] Ni,[43] Cu,[43] and Zn,[44] respectively).

In general, OER on an oxide surface occurs via four discrete electron transfer steps as:

$$* + H_2O \rightarrow *OH + H^+ + e^- \tag{2}$$

$$*OH \rightarrow *O + H^+ + e^- \tag{3}$$

$$^*O + H_2O \rightarrow {}^*OOH + H^+ + e^- \tag{4}$$

$$^*OOH \rightarrow {}^* + O_2 + H^+ + e^- \tag{5}$$

where * denotes the surface site surface; and $^*O$, $^*OH$, and $^*OOH$ indicate adsorbed species on the active site. The theoretical overpotential (η) is calculated as:

$$\eta = \max\left[\Delta G_1, \Delta G_2, \Delta G_3, \Delta G_4\right]/e - 1.23\,\text{V} \tag{6}$$

where $\Delta G_{1\text{-}4}$ denotes the reaction free energies of four electron OER paths in Equations (1)–(4).

Materials: Chromium(III) nitrate nonahydrate and cobalt(II) nitrate were produced by Sigma–Aldrich. Sodium tungstate was purchased from Merck.

Synthesis of M-WO$_4$ OER Catalysts: To make $Cr_{0.1}Co_{0.9}WO_4$, a mixed solution of $Cr(NO_3)_3$ and $Co(NO_3)_2$ was slowly added dropwise to a 35 mL 0.1 M Na_2WO_4 solution for 1 h, resulting in the addition of 0.1 equivalent of Cr and 0.9 equivalent of Co compared to Na_2WO_4. After mixing the metal nitrate and sodium tungstate solutions, an autoclave was conducted at 180 °C for 12 h at 180 °C. For $CoWO_4$, 0.1 M $Co(NO_3)_2$ was added dropwise to 0.1 M Na_2WO_4 for 1 h, while maintaining the pH at 7.0 during the precipitation process. The resulting mixture underwent hydrothermal treatment at 180 C for 12 h. Subsequently, the purple powder was annealed at 450 °C for 4 h.

Characterizations and Electrochemical Characterizations: The electrochemical performance was evaluated using linear-sweep voltammetry and cyclic voltammetry with a scan rate of 5 mV s^{-1} in a three-electrode configuration: Ag/AgCl as a reference electrode, Pt wire as a counter electrode, and our sample as a working electrode using a VSP potentiostat/galvanostat (Bio-Logics Science Instruments, France) in 1.0 M KOH (pH 14). For working electrode, 200 mg mL^{-1} catalysts in an isopropyl alcohol/Nafion mixture (9:1, v/v) were drop-casted onto the glassy carbon electrode (GCE). The ORR performance was measured using rotating ring (Pt)-disk (glassy carbon) electrode under the following configuration: a reference electrode, Ag/AgCl; a counter electrode, Pt coil; electrolyte, 0.1 M KOH saturated with O$_2$; 10 mV s^{-1}, scan rate. The 3 mM catalyst with 10% Ketjen black was drop-casted onto the disk electrode. The electron transfer number was calculated following Equation (6):

$$\text{Electron transfer number} = \frac{4I_d}{I_d + I_r/N} \tag{7}$$

Supporting Information

Supporting Information is available from the Wiley Online Library or from the author.

Acknowledgements

Conflict of Interest

The authors declare no conflict of interest.

Data Availability Statement

The data that support the findings of this study are available in the supplementary material of this article.

[1] I. E. L. Stephens, J. Rossmeisl, I. Chorkendorff, *Science* **2016**, *354*, 1378.
[2] X. Zhang, X.-G. Wang, Z. Xie, Z. Zhou, *Green Energy Environ.* **2016**, *1*, 4.
[3] Z.-L. Wang, D. Xu, J.-J. Xu, X.-B. Zhang, *Chem. Soc. Rev.* **2014**, *43*, 7746.
[4] H. Dau, C. Limberg, T. Reier, M. Risch, S. Roggan, P. Strasser, *ChemCatChem* **2010**, *2*, 724.
[5] Y. Lee, J. Suntivich, K. J. May, E. E. Perry, Y. Shao-Horn, *J. Phys. Chem. Lett.* **2012**, *3*, 399.
[6] F. Lu, J. Sui, J. Su, C. Jin, M. Shen, R. Yang, *J. Power Sources* **2014**, *271*, 55.
[7] Y. Zhu, S. Liu, C. Jin, S. Bie, R. Yang, J. Wu, *J. Mater. Chem. A* **2015**, *3*, 13563.
[8] M. Bajdich, M. García-Mota, A. Vojvodic, J. K. Nørskov, A. T. Bell, *J. Am. Chem. Soc.* **2013**, *135*, 13521.
[9] S. M. Montemayor, A. F. Fuentes, *Ceram. Int.* **2004**, *30*, 393.
[10] Y. Ji, L. Yang, X. Ren, G. Cui, X. Xiong, X. Sun, *ACS Sustainable Chem. Eng.* **2018**, *6*, 9555.
[11] S. M. AlShehri, J. Ahmed, T. Ahamad, P. Arunachalam, T. Ahmad, A. Khan, *RSC Adv.* **2017**, *7*, 45615.
[12] R. Wu, J. Zhang, Y. Shi, D. Liu, B. Zhang, *J. Am. Chem. Soc.* **2015**, *137*, 6983.
[13] C. Shu, S. Kang, Y. Jin, X. Yue, P. K. Shen, *J. Mater. Chem. A* **2017**, *5*, 9655.
[14] B. J. Rani, G. Ravi, S. Ravichandran, V. Ganesh, F. Ameen, A. Al-Sabri, R. Yuvakkumar, *Appl. Nanosci.* **2018**, *8*, 1241.
[15] M. K. Adak, A. Rajput, L. Mallick, B. Chakraborty, *ACS Appl. Energy Mater.* **2022**, *5*, 5652.
[16] R. R. Katzbaer, W. M. Vincent, Z. Mao, R. E. Schaak, *Inorg. Chem.* **2023**, *62*, 7843.
[17] N. Tsvetkov, Q. Lu, L. Sun, E. J. Crumlin, B. Yildiz, *Nat. Mater.* **2016**, *15*, 1010.
[18] G. Chen, Z. Hu, Y. Zhu, Z.-G. Chen, Y. Zhong, H.-J. Lin, C.-T. Chen, L. H. Tjeng, W. Zhou, Z. Shao, *J. Mater. Chem. A* **2018**, *6*, 9854.
[19] B. Zhang, L. Wang, Z. Cao, S. M. Kozlov, F. P. García de Arquer, C. T. Dinh, J. Li, Z. Wang, X. Zheng, L. Zhang, *Nat. Catal.* **2020**, *3*, 985.
[20] Y. Tang, Y.-G. Wang, J. Li, *J. Phys. Chem. C* **2017**, *121*, 11281.
[21] X. Li, P. Cui, W. Zhong, J. Li, X. Wang, Z. Wang, J. Jiang, *Chem. Commun.* **2016**, *52*, 13233.
[22] A. Grimaud, K. J. May, C. E. Carlton, Y.-L. Lee, M. Risch, W. T. Hong, J. Zhou, Y. Shao-Horn, *Nat. Commun.* **2013**, *4*, 2439.
[23] J. R. Petrie, V. R. Cooper, J. W. Freeland, T. L. Meyer, Z. Zhang, D. A. Lutterman, H. N. Lee, *J. Am. Chem. Soc.* **2016**, *138*, 2488.
[24] Y.-L. Lee, J. Kleis, J. Rossmeisl, Y. Shao-Horn, D. Morgan, *Energy Environ. Sci.* **2011**, *4*, 3966.
[25] C. Ling, L. Q. Zhou, H. Jia, *RSC Adv.* **2014**, *4*, 24692.

[26] I. C. Man, H. Y. Su, F. Calle-Vallejo, H. A. Hansen, J. I. Martínez, N. G. Inoglu, J. Kitchin, T. F. Jaramillo, J. K. Nørskov, J. Rossmeisl, *Chem-CatChem* **2011**, *3*, 1159.

[27] J. Rossmeisl, Z.-W. Qu, H. Zhu, G.-J. Kroes, J. K. Nørskov, *J. Electroanal. Chem.* **2007**, *607*, 83.

[28] J. Rossmeisl, A. Logadottir, J. K. Nørskov, *Chem. Phys.* **2005**, *319*, 178.

[29] A. T. Marshall, L. Vaisson-Béthune, *Electrochem. Commun.* **2015**, *61*, 23.

[30] R. Jacobs, T. Mayeshiba, J. Booske, D. Morgan, *Adv. Energy Mater.* **2018**, *8*, 1702708.

[31] A. Grimaud, O. Diaz-Morales, B. Han, W. T. Hong, Y.-L. Lee, L. Giordano, K. A. Stoerzinger, M. T. Koper, Y. Shao-Horn, *Nat. Chem.* **2017**, *9*, 457.

[32] J. T. Mefford, X. Rong, A. M. Abakumov, W. G. Hardin, S. Dai, A. M. Kolpak, K. P. Johnston, K. J. Stevenson, *Nat. Commun.* **2016**, *7*, 11053.

[33] Y. Sun, H. Liao, J. Wang, B. Chen, S. Sun, S. J. H. Ong, S. Xi, C. Diao, Y. Du, J.-O. Wang, *Nat. Catal.* **2020**, *3*, 554.

[34] Z. Wang, W. Liu, Y. Hu, M. Guan, L. Xu, H. Li, J. Bao, H. Li, *Appl. Catal. B* **2020**, *272*, 118959.

[35] W. Gou, M. Zhang, Y. Zou, X. Zhou, Y. Qu, *ChemCatChem* **2019**, *11*, 6008.

[36] D. Xu, M. B. Stevens, Y. Rui, G. DeLuca, S. W. Boettcher, E. Reichmanis, Y. Li, Q. Zhang, H. Wang, *Electrochim. Acta* **2018**, *265*, 10.

[37] L. Bai, X. Wen, J. Guan, *ACS Appl. Energy Mater.* **2019**, *2*, 5584.

[38] G. Kresse, D. Joubert, *Phys. Rev. B* **1999**, *59*, 1758.

[39] G. Kresse, J. Furthmüller, *Comput. Mater. Sci.* **1996**, *6*, 15.

[40] J. P. Perdew, K. Burke, M. Ernzerhof, *Phys. Rev. Lett.* **1996**, *77*, 3865.

[41] S. L. Dudarev, G. A. Botton, S. Y. Savrasov, C. Humphreys, A. P. Sutton, *Phys. Rev. B* **1998**, *57*, 1505.

[42] E. Finazzi, C. Di Valentin, G. Pacchioni, A. Selloni, *J. Chem. Phys.* **2008**, *129*, 154113.

[43] A. Jain, G. Hautier, S. P. Ong, C. J. Moore, C. C. Fischer, K. A. Persson, G. Ceder, *Phys. Rev. B* **2011**, *84*, 045115.

[44] G.-Y. Huang, C.-Y. Wang, J.-T. Wang, *Comput. Phys. Commun.* **2012**, *183*, 1749.